ANALYTICAL SCIENCES MAY 2015, VOL. 31

Original Papers

Temporal Changes of Fractionation Index Caused by Changes in the Large Size of Ablated Particles in Laser Ablation–Inductively Coupled Plasma Mass Spectrometry

Ryo MACHIDA, Takashi NAKAZAWA,† and Naoki FURUTA†

Faculty of Science and Engineering, Department of Applied Chemistry, Chuo University, 1-13-27 Kasuga, Bunkyo, Tokyo 112–8551, Japan

To elucidate mechanisms of elemental fractionation that are observed in laser ablation–inductively coupled plasma mass spectrometry, the relative intensities of 34 elements, each normalized by a Ca internal standard, were measured every minute during a 10-min laser ablation of an NIST 610 glass standard. Temporal changes in the fractionation index (FI) were obtained by dividing the relative intensity of every minute by that of the first minute. The particles generated by laser ablation were collected on a filter every minute, and they were observed using scanning electron microscopy to investigate changes in the large size of particles. Large variations among the large size of particles were observed using single-site mode and under 1.0 mm defocus conditions. The 34 measured elements were classified into two groups, depending on their observed FI variation. The FI variation was rationalized by elemental behavior due to changes in the large size of ablated particles introduced into the ICP.

Keywords Elemental fractionation, laser ablation, ICP-MS, NIST glass, fractionation index, large ablated particles, SEM, defocus

(Received September 16, 2014; Accepted February 16, 2015; Published May 10, 2015)

Introduction

Laser ablation–inductively coupled plasma mass spectrometry (LA-ICPMS) is an effective sample introduction technique that has been applied to multi-elemental analysis in solids. However, LA-ICPMS suffers from elemental fractionation,[1-2] a phenomenon in which the elements in a sample are enriched (or depleted) by LA and ICP, depending on the elemental properties. Although interactions between the laser and the sample surface have gradually come to be understood,[1] the underlying causes of elemental fractionation have not been elucidated clearly.

Elemental fractionation can be quantitatively evaluated in terms of the fractionation index (FI). The FI shows how the intensity ratios of elements change in particles generated by the LA; for example, Ca intensity is often used as an internal standard in the case of measuring NIST glasses.[3-5] Research in recent years has focused on how the wavelength, repetition rate and the pulse width of the laser affect the FI.[6-7] These studies have suggested that a short wavelength, such as the 193 nm wavelength of an excimer laser, can decrease the amount of elemental fractionation. Short (femtosecond) pulse widths also have been reported to enable stoichiometric, non-thermal ablation and to yield smaller particles than those generated by lasers with longer pulse widths.[8-10]

Fundamental mechanisms of laser ablation, such as vaporization, ionization, and generation of particles, have been studied in efforts to achieve stoichiometric ablation, and ionization mechanisms in ICP also have been investigated.[11-17] It has been reported that when particles generated by LA were introduced into the ICP, mass-load-dependent matrix effects were caused in LA-ICPMS.[4] Therefore, various quantitative strategies using LA-ICPMS have been developed.[18-22] To better understand the relationship between the elements in ICP, and the number and the size of particles observed in LA-ICPMS, researchers have suggested that internal-standard elements should be chosen with the selection criterion that the LA-ICPMS behavior of these elements be the same as that of the target elements. This information will be useful for quantitative analysis with high accuracy.

In this work, in order to achieve an understanding of the relationship between FI and elemental properties, temporal changes in the FI of ablated particles were monitored. First, temporal changes in the FI were studied for a wide range of elements monitored during 10 min of laser ablation using single-site or line-scan mode and under in-focus, 0.5 mm defocus, or 1.0 mm defocus conditions. Second, to measure changes of ablated particles, the ablated particles were collected on a membrane filter, and the number of particles larger than 2 μm as well as the largest particle size for each sample was measured by means of scanning electron microscopy (SEM).

Experimental

Instrumentation

A laser ablation system (UP213, ESI, Portland, OR) in combination with ICPMS (Agilent 7500ce, Agilent Technologies,

† To whom correspondence should be addressed.
E-mail: t-nakaz@kc.chuo-u.ac.jp (T. N.); nfuruta@chem.chuo-u.ac.jp (N. F.)

Table 1 Operating conditions used for laser ablation and ICPMS measurements

Laser model	UP213
Laser type	Nd:YAG
Wavelength	213 nm
Pulse width	4 ns
Ablation mode	Single-site, Line-scan
Repetition rate	20 Hz
Carrier gas	Helium
Carrier gas flow (He)	1.0 L min^{-1}

Laser power and laser power density			
	Laser power/mJ	Diameter of crater/μm	Fluence/ J cm^{-2}
Single-site mode			
in-focus	1.3	100	16*
0.5 mm defocus	1.3	60	46*
1.0 mm defocus	1.3	200	4*
Line-scan mode			
in-focus	1.3	100	16
1.0 mm defocus	1.3	200	4

* Asterisk indicates an initial value of fluence. The actual fluence was changed with time.

ICPMS model	Agilent 7500ce
RF power	1600 W
Integration time	0.05 s
Additional gas flow (Ar)	0.8 L min^{-1}
Collision gas (He)	2 mL min^{-1}
Isotopes measured	^{24}Mg, ^{27}Al, ^{29}Si, ^{42}Ca, ^{45}Sc, ^{49}Ti, ^{52}Cr, ^{55}Mn, ^{59}Co, ^{60}Ni, ^{63}Cu, ^{66}Zn, ^{69}Ga, ^{75}As, ^{82}Se, ^{88}Sr, ^{89}Y, ^{90}Zr, ^{107}Ag, ^{111}Cd, ^{120}Sn, ^{121}Sb, ^{125}Te, ^{137}Ba, ^{140}Ce, ^{157}Gd, ^{173}Yb, ^{178}Hf, ^{184}W, ^{185}Re, ^{208}Pb, ^{209}Bi, ^{232}Th, ^{238}U

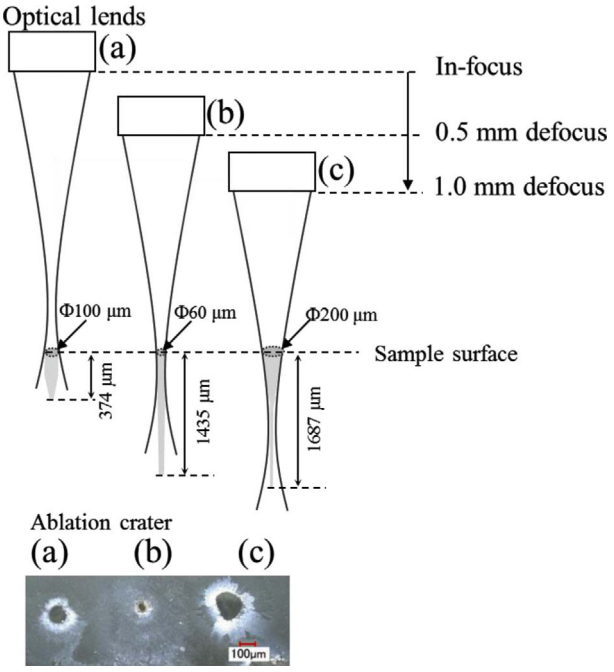

Fig. 1 Schematic diagram of the flat-top laser and ablation craters formed under different focus conditions of: (a) in-focus, (b) 0.5 mm defocus, and (c) 1.0 mm defocus.

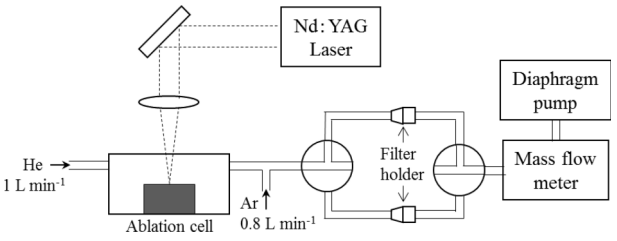

Fig. 2 Schematic diagram of experimental setup to collect ablated particles at 1-min intervals on two filters alternatively.

Tokyo, Japan) was used in this study. NIST 610 (National Institute of Standards and Technology, Gaithersburg, MD) glass standard material was used to generate samples. NIST 610 contains 61 trace elements each at a concentration of approximately 500 mg kg^{-1}, and its matrix composition is 72% SiO_2, 12% CaO, 14% Na_2O, and 2% Al_2O_3. A large format cell with 6-sq.-in. was used for a laser ablation cell. To reduce wash-out time, a quartz ring with a volume of approximately 0.8 cm^3 was mounted just above the sample. High purity He gas was flowed into the inlet of the large format cell at 1.0 L min^{-1}. Ablated particles were produced under He atmosphere. Ar gas was admixed with He at a flow rate of 0.8 L min^{-1} after the ablation cell *via* a Y-shape gas line. Ablated particles were carried by He and Ar gas mixtures into the ICP.

LA-ICPMS measurement

The LA-ICPMS measurement conditions used in this study are summarized in Table 1. The LA-ICPMS was tuned so as to provide the highest sensitivity for isotopes of ^{59}Co, ^{139}La, and ^{232}Th by using NIST 612 glass standard. The laser power (1.3 mJ) and the repetition rate (20 Hz) were used in this study because these conditions enable large enough signal to detect by LA-ICPMS. The isotopes ^{24}Mg, ^{27}Al, ^{29}Si, ^{42}Ca, ^{45}Sc, ^{49}Ti, ^{52}Cr, ^{55}Mn, ^{59}Co, ^{60}Ni, ^{63}Cu, ^{66}Zn, ^{69}Ga, ^{75}As, ^{82}Se, ^{88}Sr, ^{89}Y, ^{90}Zr, ^{107}Ag, ^{111}Cd, ^{120}Sn, ^{121}Sb, ^{125}Te, ^{137}Ba, ^{140}Ce, ^{157}Gd, ^{173}Yb, ^{178}Hf, ^{184}W, ^{185}Re, ^{208}Pb, ^{209}Bi, ^{232}Th, and ^{238}U were measured using single site mode and under in-focus, 0.5 mm defocus, and 1.0 mm defocus conditions (Fig. 1). In the case of 0.5 mm defocus and 1.0 mm defocus conditions, the laser was defocused by focusing it 0.5 or 1.0 mm beneath the sample surface based on the CCD image. Under 1.5 mm defocus conditions, no signal was observed by LA-ICPMS. So in-focus, 0.5 mm defocus, and 1.0 mm defocus conditions were adopted for understanding trends of defocus conditions. As 34 isotopes were measured with an integration time of 0.05 s, each isotope was measured with an interval of 2 s.

When the focus was changed from in-focus, 0.5 mm defocus, and 1.0 mm defocus, the crater size was changed to 100, 60, and 200 μm, respectively. Therefore, the fluence was also changed to 16, 46, and 4 J cm^{-2} depending on the crater size. In the next, ^{75}As, ^{88}Sr, ^{90}Zr, and ^{42}Ca (as an internal standard) were measured using line-scan mode and under in-focus and 1.0 mm defocus conditions.

Particle sampling and SEM observation

A schematic diagram of experimental setup for collecting

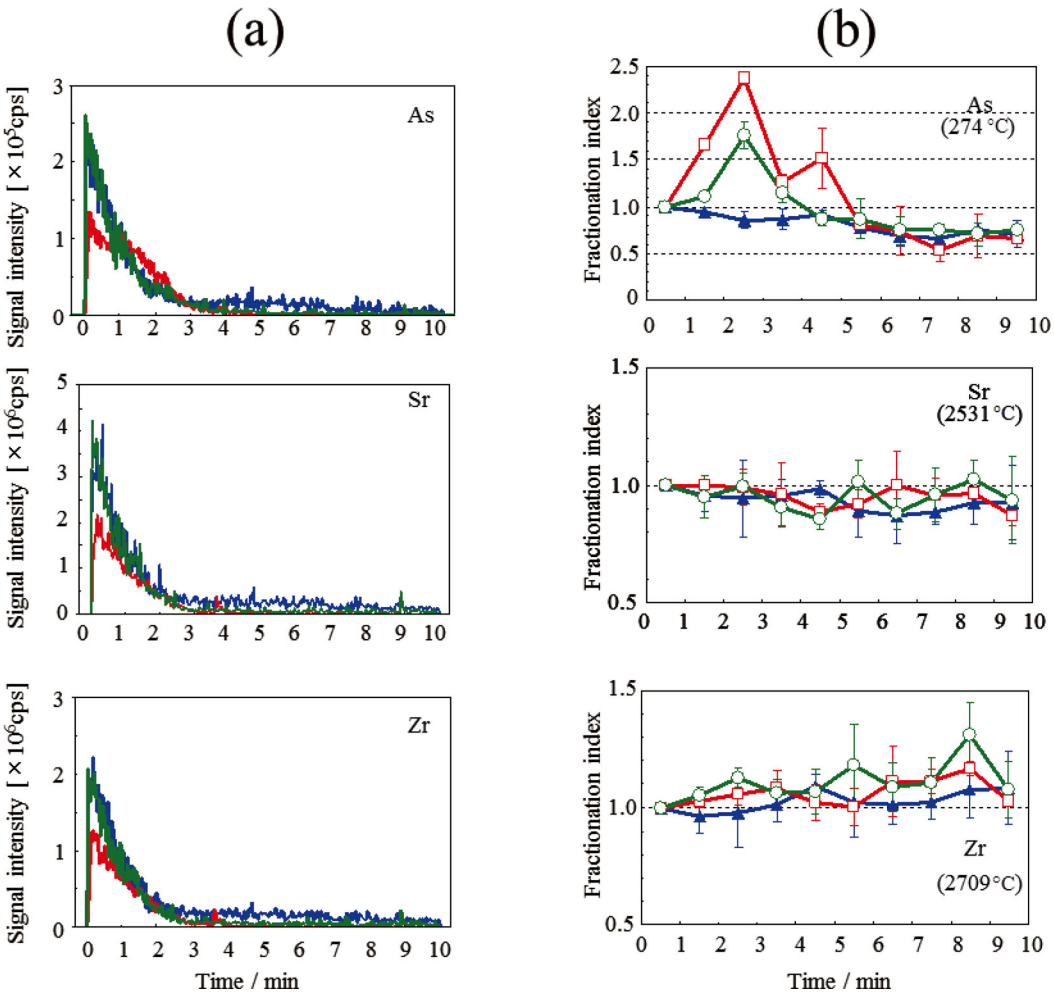

Fig. 3 (a) Signal intensities for As, Sr, and Zr obtained by LA-ICPMS. Laser ablation was performed using single-site ablation mode and under different focus conditions. —, in-focus with 16 J cm^{-2}; —, 0.5 mm defocus with 46 J cm^{-2}; —, 1.0 mm defocus with 4 J cm^{-2}; (b) The FI of As, Sr, and Zr during ablation for 10 min. -▲-, in-focus with 16 J cm^{-2}; -□-, 0.5 mm defocus with 46 J cm^{-2}; -○-, 1.0 mm defocus with 4 J cm^{-2}. The temperature in parentheses indicates the melting point of each element's corresponding metal oxide.

ablated particles is shown in Fig. 2. Ablated particles were directly collected on a nitrocellulose membrane filter (pore size: 0.45 µm, diameter: 13 mm, Waters, Milford, MA). The filter was mounted on a syringe filter holder (Millipore, Darmstadt, Germany). The ablated particles in He and Ar gas mixture were sacked from the large format cell at 1.8 L min^{-1} by means of a diaphragm pump (FTP-10B, KNF, Tokyo, Japan) equipped with a mass flow controller (Azbil Co., Tokyo, Japan). An NIST 610 glass was ablated using either single-site mode or line-scan mode during 10 min. In order to collect the ablated particles every minute, T-shape valves were used to switch two filter holders every minute. The filter was replaced every minute.

A scanning electron microscope (SEM; S-4300, Hitachi High Technologies, Tokyo, Japan) was performed to observe the number and the size of ablated particles. The filter surface was coated with a Pt/Pd alloy by ion sputtering (E-1045, Hitachi High Technologies). The largest three ablated particles were searched from all over the filter surface and SEM images of a rectangular area of 500 µm by 380 µm were obtained around the largest particle with a magnification of 250.

The number and the size of ablated particles were measured by counting the particles with diameters of larger than 2 µm and also by noting the largest-size particle observed in the rectangular area of 500 µm by 380 µm. Ablated particles with diameters larger than 2 µm were counted as a particle clearly. Spherical, agglomerated, and edge-shaped particles were observed in ablated particles less than 2 µm. Edge-shaped particles were mainly observed in ablated particles larger than 2 µm.

Crater shape monitoring

Detailed examination of the crater size and depth has been carried out using an optical microscope (VHX-2000, Keyence, Osaka, Japan). Crater size and depth were measured by observation of sample surface and side, respectively, after laser irradiation. The drilling rate of laser ablation was determined by measuring the depths of craters created by laser ablation every minute.

Results and Discussion

Single-site mode

Using single-site mode and under in-focus, 0.5 mm defocus, and 1.0 mm defocus conditions, the elemental intensities of As,

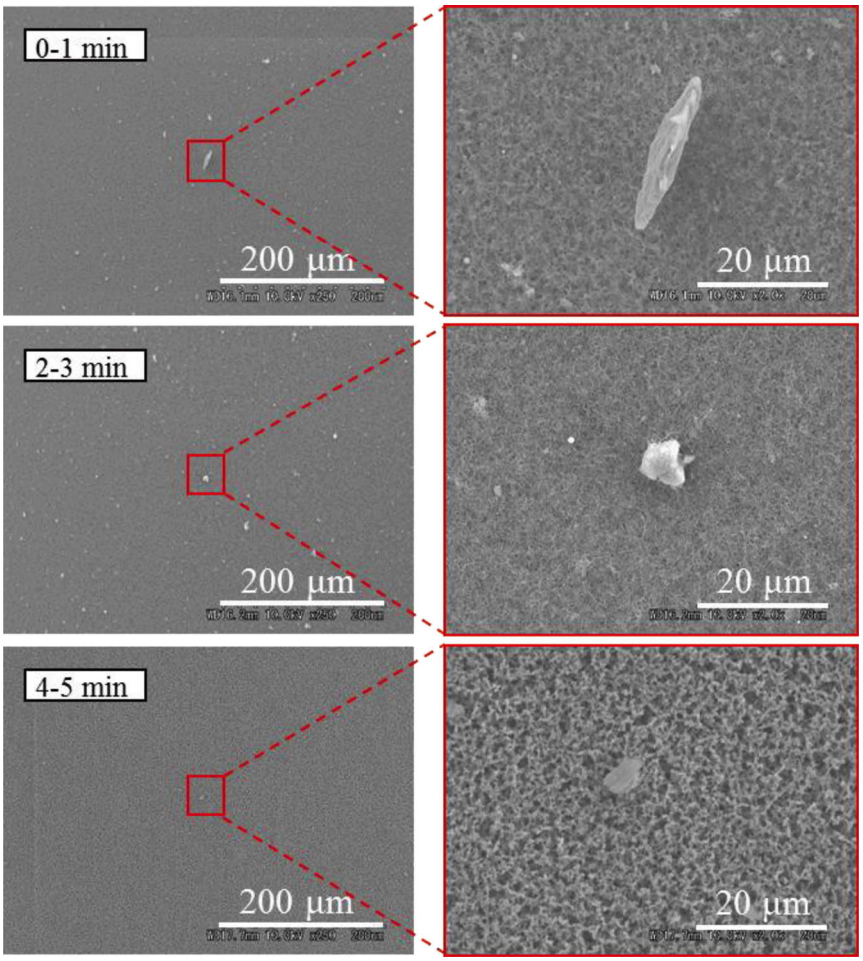

Fig. 4 SEM images of particles collected at 1-min intervals during laser ablation using single-site mode and under in-focus conditions with 16 J cm^{-2}.

Ca, Sr, and Zr were measured by means of time-resolved analysis. Under in-focus, 0.5 mm defocus, and 1.0 mm defocus conditions, the fluence were 16, 46, and 4 J cm^{-2}, respectively, depending on the crater size (Fig. 1), while the laser power was fixed at 1.3 mJ. The signal intensities of As, Sr, and Zr as a function of ablation time are shown in Fig. 3(a). For this set of experiments, As, Sr, and Zr were selected as typical elements, in accordance with the classification of elements described in the later chapter of "*Classification of elements*".

For laser ablation using single-site mode under 16, 46, and 4 J cm^{-2} fluences, the signal intensities of all measured elements decreased with time because increasing the depth of the crater pit made it difficult for the ablated particles to fly out from the crater pit, and the drilling amount decreased with an increase in the depth of the pit. From Fig. 3(a), the FI was calculated from the following Eq. (1):

$$\mathrm{FI} = \frac{\sum \mathrm{cps}\,(\mathrm{M}_{\Delta 1\,\mathrm{min}}) / \sum \mathrm{cps}\,(\mathrm{Ca}_{\Delta 1\,\mathrm{min}})}{\sum \mathrm{cps}\,(\mathrm{M}_{0\text{-}1\,\mathrm{min}}) / \sum \mathrm{cps}\,(\mathrm{Ca}_{0\text{-}1\,\mathrm{min}})} \quad (1)$$

where cps ($M_{\Delta 1\ min}$) and cps (Ca $\Delta_{1\ min}$) are the signal intensities of an element and Ca, respectively, observed every minute during the 10-min ablation period; and cps ($M_{0\text{-}1\ min}$) and cps ($Ca_{0\text{-}1\ min}$) are the signal intensities of the element and Ca, respectively, observed during only the first minute of ablation. The FI of As, Sr, and Zr as a function of ablation time are shown in Fig. 3(b). LA-ICPMS measurements and calculation of the FI were repeated three times and an error bar of FI is shown in Fig. 3(b).

In the case of in-focus conditions, for As, the FI decreased to 0.7 at 10 min. In contrast, the FI for Sr and Zr remained mostly constant during the 10-min ablation process. The FI of As increased to 2.4 at 3 min under 0.5 mm defocus conditions and increased to 1.8 at 3 min under 1.0 mm defocus conditions; the FI then decreased under both defocus conditions. For Sr, the FI under defocus conditions exhibited the same trends as those observed under in-focus conditions. The FI of Zr increased slightly to 1.1 under 0.5 mm defocus and 1.0 mm defocus conditions.

We concluded that the differences in FI observed for these three elements were likely related to differences in their elemental properties, including melting point and boiling point. For example, As is more volatile than the reference Ca, whereas the elemental properties of Sr are similar to those of Ca, which probably explains why the FI for Sr remained mostly constant during ablation. Elements with high melting and boiling points, such as Zr, probably were difficult to vaporize in the ICP during the first minute of ablation before becoming more efficiently vaporized with increasing time, thus explaining the observed FI behavior for Zr.

Guillong and Günther[15] and Guillong *et al.*[23] reported that the excitation process within the ICP, such as vaporization, atomization, and ionization, was influenced by the size of ablated particles. Therefore, we assumed that the temporal

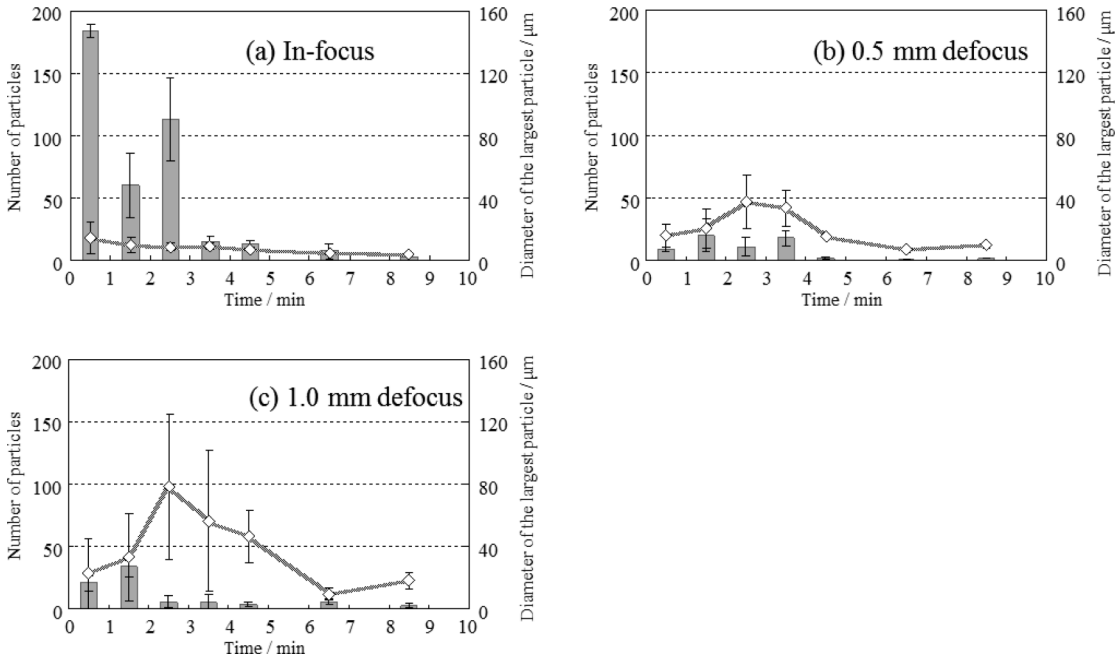

Fig. 5 The number of particles larger than 2 μm and the diameter of the largest particle observed in SEM images of laser-ablated particles obtained under single-site mode, and (a) in-focus, (b) 0.5 mm defocus, and (c) 1.0 mm defocus conditions with 16, 46, and 4 J cm^{-2}, respectively. ■, Number of particles; ◇, Diameter of the largest particle. Error bars indicate standard deviation (n = 3).

changes of FI observed in this study were related to the size of ablated particles. In order to investigate the possible effect of temporal changes in particle size on the observed FI, we acquired SEM images of the particles generated by laser ablation. The particles generated by laser ablation were collected on a filter every minute. SEM images of the laser-ablated particles under in-focus conditions (each image is a rectangular area of 500 μm by 380 μm) are shown on the left side of Fig. 4. Regions of interest in these images (red boxes in Fig. 4, left) were magnified 10× to acquire additional SEM images (Fig. 4, right). These images clearly show that the number of particles collected on the filter decreased and that the particle size also decreased with increasing ablation time.

The number of particles larger than 2 μm, as well as the largest particle observed, were recorded for each SEM-imaged rectangular area. The number of particles and the diameter of the largest particle are shown in Figs. 5(a) – 5(c). SEM image measurements at 5 – 6, 7 – 8, and 9 – 10 min did not show any remarkable change.

Under in-focus conditions, we observed an average of 184 ± 5 particles larger than 2 μm at 0 – 1 min. The diameter of the largest particle observed in this set of images was 14.0 ± 10.2 μm. The number of particles larger than 2 μm and the diameter of the largest particle observed decreased with increasing ablation time. After 8 – 9 min, only 3 ± 3 particles larger than 2 μm were observed, and the diameter of the largest particle was 3.9 ± 0.7 μm.

To explain these observed decreases in particle size, we again considered differences in elemental properties among the elements. Arsenic (As) was ionized more easily than Ca, because As oxide has a much lower melting point (274°C) than Ca oxide (2570°C). The generation of smaller particles increased after 1 min ablation, and then the Ca in these particles was easily ionized in the ICP. As the size of the ablated particles decreased, the rate of ionization of Ca increased relative to that of As. In contrast, the FI of Sr remained constant with time, because Sr, an alkaline earth metal like Ca, has an oxide melting point (2531°C) similar to that of Ca oxide. The melting point of Zr oxide (2709°C) is higher than that of Ca oxide (2570°C), and therefore Zr was more difficult to vaporize in the ICP than Ca. This difference between melting points of Zr oxide and Ca oxide exerted the largest influence on particles larger than 2 μm. With increasing ablation time, the diameter of the ablated particles became smaller, and that induced that vaporization efficiency of refractory elements was improved more than that of Ca. Therefore, the FI of Zr slightly increased with ablation time.

Volatile elements in the particles were easily vaporized in the ICP regardless of particle size. Refractory elements such as Zr in particles were difficult to vaporize in the ICP, however these elements became easy to vaporize with decreasing particle size. We concluded that this particle-size-dependent vaporization was one of the mechanisms that contributed to the observed differences in elemental fractionation.

In the case of 1.0 mm defocus conditions with 4 J cm^{-2}, as shown in Fig. 5(c), the largest particle observed on filters collected at 1 – 2, 2 – 3, 3 – 4, and 4 – 5 min were larger than those collected at 0 – 1 min, in contrast to the particle-size trend observed for particles collected under in-focus conditions (Fig. 5(a)). The diameter of the largest particles collected at 1 – 2, 2 – 3, and 3 – 4 min under 0.5 mm defocus conditions were also larger than those collected at 0 – 1 min (Fig. 5(b)).

The signal intensity and the FI of As (shown in Fig. 3) as a function of crater depth is shown in Fig. 6(a). The crater depth observed every minute and a microscope image of the crater after 10 min ablation under 1.0 mm defocus conditions are shown in Figs. 6(b) and 6(c), respectively. In the case of defocus conditions, actual laser fluence increased due to crater size decrease as the ablation process progressed. It is considered that the higher fluence generated larger shockwave, and then

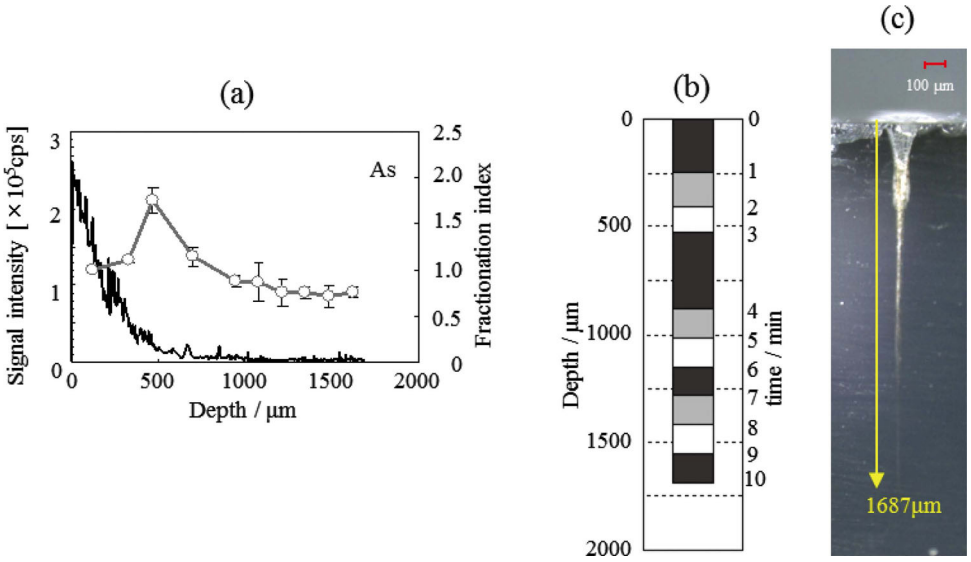

Fig. 6 (a) Signal intensities and FI of As obtained by LA-ICPMS. Laser ablation was performed using single-site mode and under 1.0 mm defocus conditions with 4 J cm^{-2}. ━, signal intensities; -○-, FI. (b) The crater depth observed every minute. (c) A microscope image of crater after 10 min ablation using single-site mode and under 1.0 mm defocus conditions with 4 J cm^{-2}.

produced large edge-shaped particles at the depth of 410 – 520 μm. As the result, the maximum value of FI was observed at 2 – 3 min (Fig. 3). The aspect ratio of 2 – 2.6 was calculated from the crater size and the depth created during 2 – 3 min ablation process.

For explanation of the observed increase in the FI for As, we presumed that Ca became difficult to ionize as the diameter of particles increased with increasing ablation time up to 5 min. The FI of As decreased below 1.0 after 5 min because the particles collected after 5 min were smaller than the particles collected at 0 – 1 min under both 0.5 and 1.0 mm defocus conditions. In this study, particles more than 2 μm were counted by using SEM, however there was a possibility that the relative number of particles less than 2 μm might increase as the ablation process progressed. Koch *et al.*[24] indicated that using femtosecond LA at fluence of <5 J cm^{-2} and generating ultra-fine aerosols (mean diameter ≈ 10 nm) led to decrease of elemental fractionation. The volume of particles with diameter of 2 μm (4×10^{-12} cm^3) is 8×10^6 times larger than that of 10 nm (5×10^{-19} cm^3). Consequently, the signal intensity within the ICP was affected by the large ablated particles. Therefore, the temporal changes in the number and the large ablated particles were one of reasons of elemental fractionation. The FI of Sr remained constant regardless of the ablated particles' number and the largest size of them. The FI of Zr slightly increased as the number of particles larger than 2 μm decreased. As mentioned above, there might be the relative number of particles less than 2 μm increase as the ablation process progressed.

Line-scan mode

Using line-scan mode and under in-focus and 1.0 mm defocus conditions, the elemental intensities of As, Sr, and Zr were measured. The signal intensities of As, Sr, and Zr as a function of ablation time are shown in Fig. 7(a). The FI was calculated from the intensity data and plotted in Fig. 7(b). When the line-scan mode was used, the FI of all elements was constant under both in-focus and 1.0 mm defocus conditions. SEM images of particles ablated using line-scan mode and under in-focus conditions at 0 – 1 and 4 – 5 min are shown in Fig. 8(a). These particle sizes observed in these SEM images are similar to those observed at 0 – 1 min using single-site mode (Fig. 4).

The number of particles larger than 2 μm and the diameter of the largest particle observed within a rectangular area of 500 μm by 380 μm are shown in Fig. 8(b). The diameter of the largest particle observed using line-scan mode was larger than that observed at 0 – 1 min using single-site mode, and the aspect ratio using line-scan mode was smaller than that of using single-site mode. These effects helped that the signal intensity was larger using line-scan mode. The number of particles and the diameter of the largest particle did not change during the ablation process. This result most likely occurred because the interaction between the laser and the sample surface would have remained nearly constant throughout the line-scan mode ablation, because the laser would have been continually scanning over unablated areas of the sample; in contrast, in single-site mode ablation the same point on the sample surface is ablated continuously, which caused the laser-sample interactions to fluctuate during ablation.

Classification of elements

The FI behavior of 34 elements in NIST 610 (which contains 65 elements total, including its matrix components) was measured using single-site mode and under 1.0 mm defocus conditions (Figs. 9 and 10). Each of the elements was classified into two groups in accordance with their observed temporal changes in FI. The classification of the elements, values of FI (during 2 – 3 min), along with the melting, and boiling points of metal oxides, bond dissociation energy (BDE), and boiling point of atomic elements[25] are listed in Table 2.

The elements Ag, As, Se, Sb, Ga, Te, Bi, Pb, Cd, Re, Sn, Cu, W, and Zn were classified in Group1 because FI values (2 – 3 min) of these were larger than over 1.20. The elements Si, Co, Mn, Ti, Ni, Ba, Al, Ce, Cr, Gd, Yb, Y, Sc, Sr, Ca, Zr, Hf, Mg, U, and Th were classified in Group 2 because FI values (2 – 3 min) of these were within 1 ± 0.15.

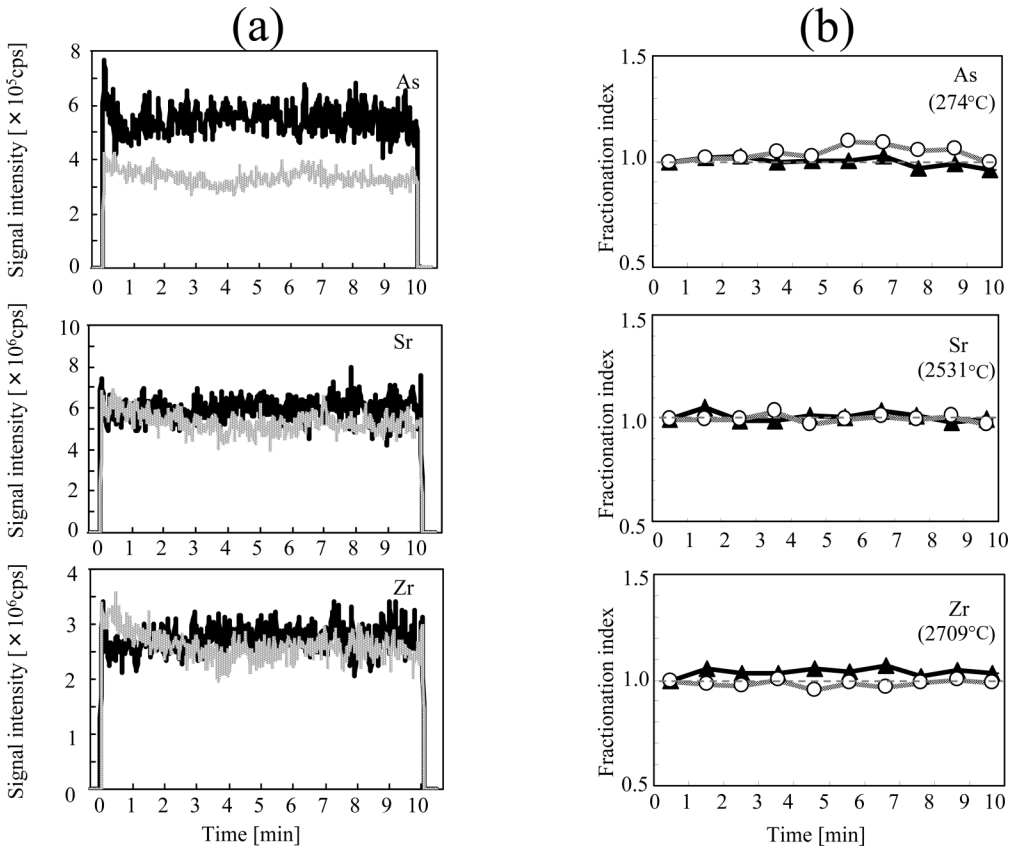

Fig. 7 (a) Signal intensities of As, Sr, and Zr obtained by LA-ICPMS. Laser ablation was performed using line-scan mode and under in-focus and 1.0 mm defocus conditions. ━, in-focus with 16 J cm^{-2}; ━, 1.0 mm defocus with 4 J cm^{-2}. (b) FI of As, Sr, and Zr during ablation for 10 min. The temperature in parentheses indicates each element's corresponding metal oxide. -▲-, in-focus with 16 J cm^{-2}; -○-, 1.0 mm defocus with 4 J cm^{-2}.

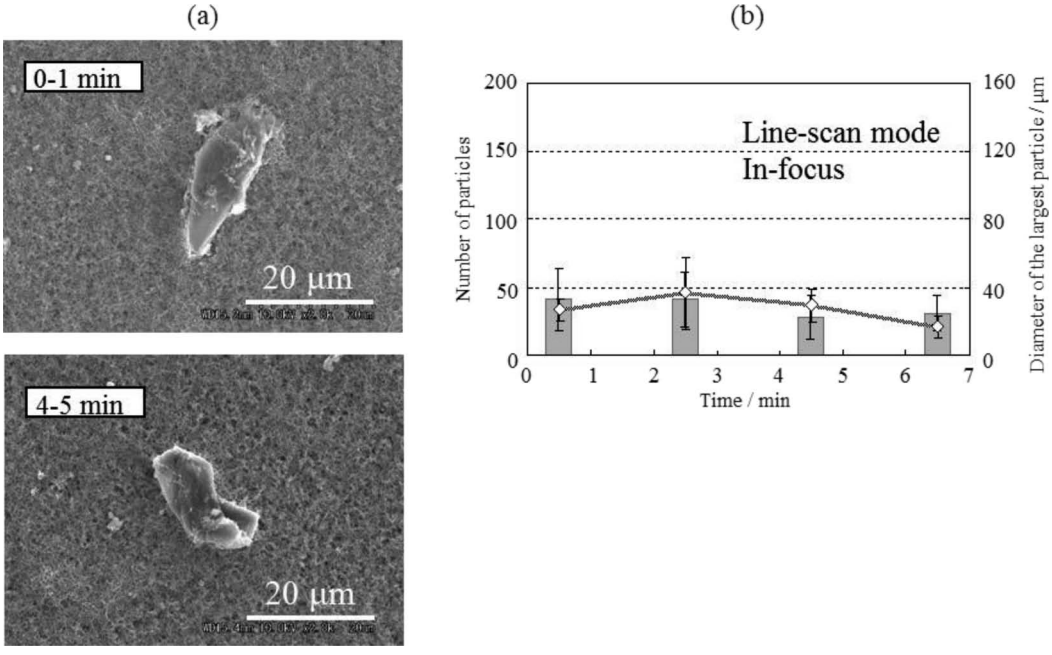

Fig. 8 (a) SEM images of particles. (b) The number of particles larger than 2 μm and the diameter of the largest particle collected at 1-min intervals during laser ablation using line-scan mode and under in-focus conditions with 16 J cm^{-2}. ■, Number of particles; ◇, Diameter of the largest particle. Error bars indicate standard deviation (n = 3).

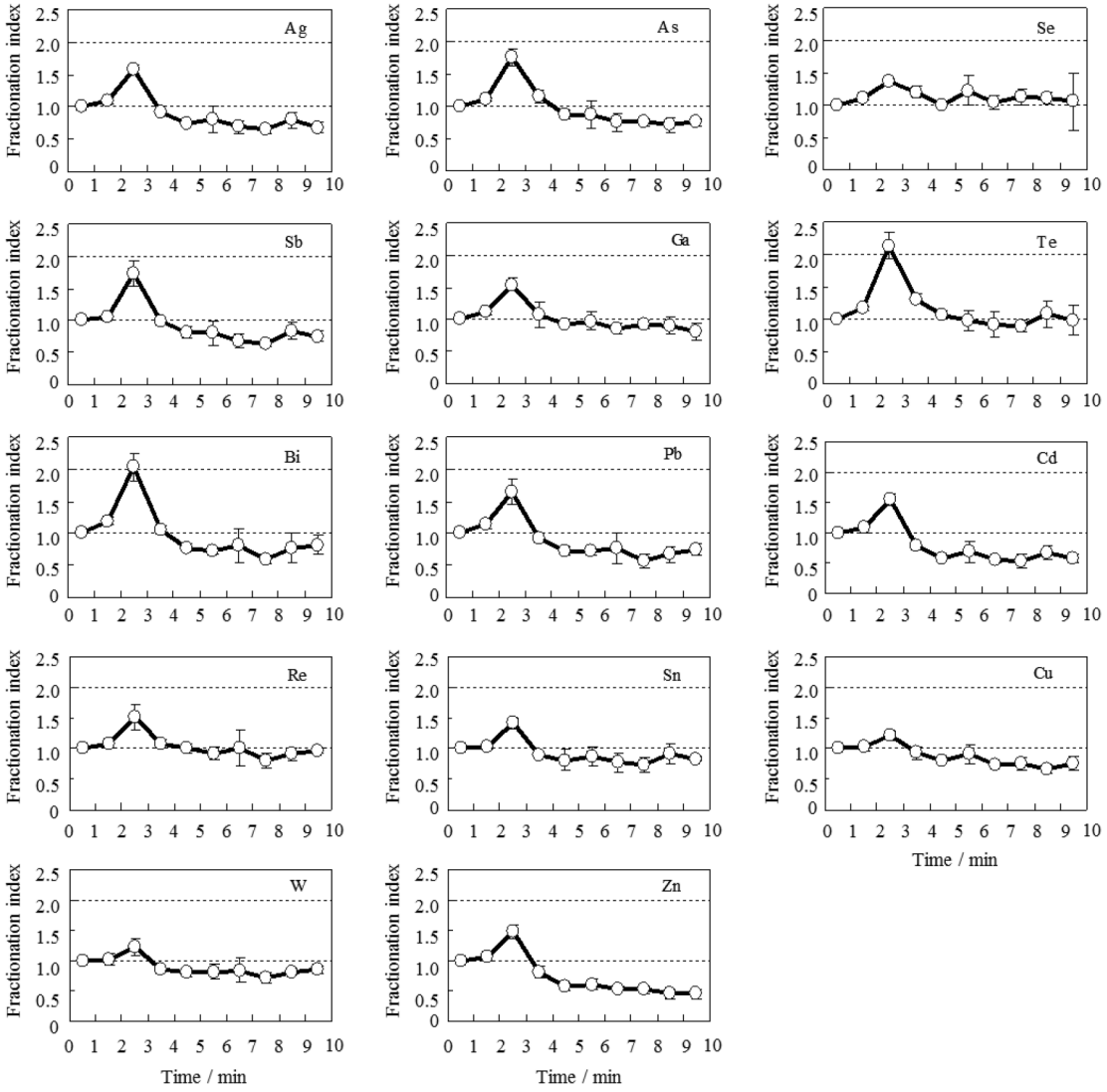

Fig. 9 Temporal changes in FI of Ag, As, Se, Sb, Ga, Te, Bi, Pb, Cd, Re, Sn, Cu, W, and Zn during laser ablation using single-site mode and under 1.0 mm defocus conditions with 4 J cm^{-2}. These elements were classified into Group 1.

As shown in Fig. 9, the FI of Ag, As, Se, Sb, Ga, Te, Bi, Pb, Cd, Re, Sn, Cu, W, and Zn showed an increasing trend until 3 min of laser ablation, at which point the FI decreased for each of these elements, in a similar manner to that observed for As (Fig. 3). The FI of these elements exceeded 1 when particles larger than those observed at 0 – 1 min of ablation were introduced into the ICP, and fell below 1 when particles smaller than those observed at 0 – 1 min of ablation were introduced into the ICP. The melting points of all metal oxides in Group 1 are lower than that of Ca oxide (Table 2). Of all the Group 1 elements, Zn oxide has the highest melting point, but because this boiling point of Zn atom is lower than that of elements classed in Group 2, Zn exhibited FI trends similar to those of the other elements in Group 1.

As shown in Fig. 10, the FI of Si, Co, Mn, Ti, Ni, Ba, Al, Ce, Cr, Gd, Yb, Y, Sc, Sr, Ca, Zr, Hf, Mg, U, and Th remained nearly constant throughout the 10-min ablation process, similar to the behavior observed for Sr and Zr (Fig. 3). The FI of these elements was constant regardless of changes in the large ablated particles, because these elements behaved similarly to Ca in the ICP. Therefore, these elements were classified into Group 2. Most of the oxides in Group 2 have higher melting points than those in Group 1.

In summary, classification of these elements from temporal changes in their FI during laser ablation using single-site mode under 1.0 mm defocus conditions enabled us to identify trends in the behavior of the elements in the ICP. Elemental fractionation was caused by large particles introduced into the ICP when fluence increased using single-site ablation mode. Under 1.0 mm defocus conditions, this phenomenon occurred when fluence increased at the depth of 410 – 520 μm. It is noticed that an appropriate selection of internal-standard element and control of laser fluence are necessary depending on the sample.

Conclusions

In this study, we measured temporal changes in the FI of ablated particles during 10 min of laser ablation under in-focus, 0.5 mm defocus, and 1.0 mm defocus conditions. In the case of volatile elements (Group 1), a remarkable peak of FI was observed at

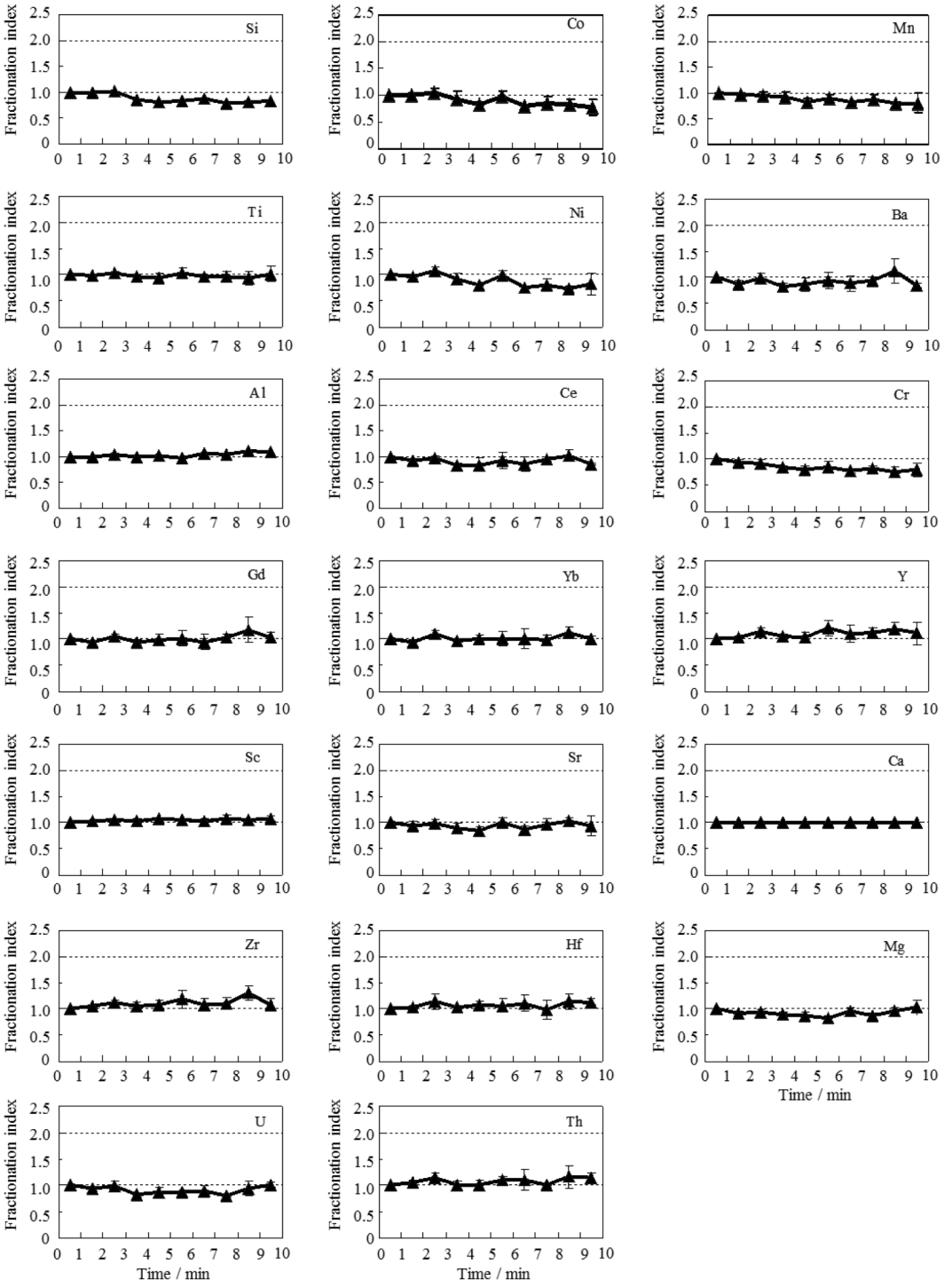

Fig. 10 Temporal changes in FI of Si, Co, Mn, Ti, Ni, Ba, Al, Ce, Cr, Gd, Yb, Y, Sc, Sr, Ca, Zr, Hf, Mg, U, and Th during laser ablation using single-site mode and under 1.0 mm defocus conditions with 4 J cm^{-2}. These elements were classified into Group 2.

2 – 3 min under 0.5 and 1.0 mm defocus conditions. The particles that were produced at 2 – 3 min were observed by SEM. The large particles more than 2 µm were monitored by SEM. It was considered that the large edge-shaped particles were produced by shockwave which was induced by an increase of fluence as the ablation process progressed. We assumed that the temporal changes of FI were caused by the large particles more than 2 µm which were related to an increase of fluence. Although, there is a possibility that the FI was affected by particles less than 2 µm. For further investigations, we need to focus on particle size distribution and chemical composition of fine particles. We are now proceeding with these experiments.

Temporal changes in FI were explained by elemental behavior due to changes in the large size of ablated particles introduced into the ICP. The FI indicated how the signal ratio of a given pair of elements (*i.e.*, a sample element and a Ca standard) in the particles generated by laser ablation changed upon introduction to the ICP. In addition, comprehensive evaluation

Table 2 Classification of 34 elements depending on their observed temporal changes in FI along with their melting point (m.p.), boiling point (b.p.), and bond dissociation energy (BDE)[25]

Element	Group	FI	Oxide				Atom
		2 – 3 min	compound	m.p./°C	b.p./°C	BDE/kJ mol^{-1}	b.p./°C
Ag	1	1.58	Ag_2O	200	—	221	2162
As	1	1.76	As_2O_3	274	460	484	603
Se	1	1.38	SeO_2	340	—	469	685
Sb	1	1.73	Sb_2O_3	570	1425	434	1587
Ga	1	1.54	Ga_2O	660	800	374	2204
Te	1	2.14	TeO_2	733	1245	377	988
Bi	1	2.03	Bi_2O_3	817	1990	337	1564
Pb	1	1.64	PbO	897	—	238	1749
Cd	1	1.54	CdO	900	1385	236	767
Re	1	1.52	ReO_2	900	—	627	5596
Sn	1	1.41	SnO	1080	—	528	2602
Cu	1	1.20	CuO_2	1235	1800	281	2562
W	1	1.23	WO_2	1500	—	832	5555
Zn	1	1.49	ZnO	1974	—	226	907
Si	2	1.01	SiO_2	1722	2950	800	3265
Co	2	1.04	CoO	1830	—	385	2927
Mn	2	0.96	MnO	1839	—	362	2061
Ti	2	1.03	TiO_2	1843	2900	668	3287
Ni	2	1.07	NiO	1955	—	366	2913
Ba	2	0.99	BaO	1972	—	562	1897
Al	2	1.04	Al_2O_3	2053	—	502	2519
Ce	2	0.98	Ce_2O_3	2210	3730	790	3443
Cr	2	0.92	Cr_2O_3	2329	3000	461	2671
Gd	2	1.06	Gd_2O_3	2339	3900	715	3273
Yb	2	1.10	Yb_2O_3	2355	4070	401	1196
Y	2	1.14	Y_2O_3	2438	—	698	3345
Sc	2	1.06	Sc_2O_3	2485	—	671	2836
Sr	2	1.00	SrO	2531	—	426	1382
Ca	2	1.00	CaO	2570	2850	383	1484
Zr	2	1.13	ZrO_2	2709	4300	766	4409
Hf	2	1.14	HfO_2	2774	—	801	4603
Mg	2	0.94	MgO	2825	3600	358	1090
U	2	0.99	UO_2	2827	—	755	4131
Th	2	1.15	ThO_2	3390	4400	877	4788

of the particle number and the size by SEM observation and of temporal changes in the FI helped to further elucidate elemental behavior in the ICP. The results of these experiments were used to classify the elements into two groups.

The elements that were classified according to temporal changes in their FI behaved differently from one another according to changes in the large ablated particles. Therefore, we concluded that changes in the large size of ablated particles are one of the main causes for elemental fractionation. To control the influence of ablated-particle size on LA-ICPMS analysis, a certified reference material with a matrix similar to that of the sample should be used for calibration. However, such certified reference materials are not always available. In the case of glass sample analysis, the results of this work should be helpful.

Selection of an appropriate internal-standard element is important to obtain accurate LA-ICPMS measurements. On the basis of our findings in this study, we recommend that an internal standard element be chosen from the same group in Table 2 as the target element because the relative signal intensities of these elements in LA-ICPMS should remain similar even if the number and the size of particles change over time. We also found that laser ablation using line-scan mode provided a means to stabilize the number and the size of ablated particles and minimize changes therein.

Acknowledgements

This research was supported by the Ministry of Education, Culture, Sports, Science and Technology, Japan, through a Grant-in-Aid for Scientific Research (C) 26410160 and Young Scientists (B) 26870595. Part of this study was supported under a joint research project conducted at the Institute of Science and Engineering of Chuo University.

References

1. R. E. Russo, X. Mao, J. J. Gonzalez, V. Zorba, and J. Yoo, *Anal. Chem.*, **2013**, *85*, 6162.
2. H. P. Longerich, D. Günther, and S. E. Jackson, *Fresenius' J. Anal. Chem.*, **1996**, *355*, 538.
3. B. J. Fryer, S. E. Jackson, and H. P. Longerich, *Can. Mineral.,* **1995**, *33*, 303.
4. I. Kroslakova and D. Günther, *J. Anal. At. Spectrom.*, **2007**, *22*, 51.
5. T. E. Jeffries, S. E. Jackson, and H. P. Longerich, *J. Anal.*

At. Spectrom., **1998**, *13*, 935.
6. M. Ohata, D. Tabersky, R. Glaus, J. Koch, B. Hattendorf, and D. Günther, *J. Anal. At. Spectrom.*, **2014**, *29*, 1345.
7. F. Claverie, B. Fernández, C. Pécheyran, J. Alexis, and O. F. X. Donard, *J. Anal. At. Spectrom.*, **2009**, *24*, 891.
8. D. Günther and C. A. Heinrich, *J. Anal. At. Spectrom.*, **1999**, *14*, 1369.
9. C. Liu, X. L. Mao, S. S. Mao, X. Zeng, R. Greif, and R. E. Russo, *Anal. Chem.*, **2004**, *76*, 379.
10. T. Hirata and Y. Kon, *Anal. Sci.*, **2008**, *24*, 345.
11. H. R. Kuhn, M. Guillong, and D. Günther, *Anal. Bioanal. Chem.*, **2004**, *378*, 1069.
12. M. Ohata and N. Furuta, *Anal. Sci.*, **2004**, *20*, 701.
13. L. Fornarini, V. Spizzichino, F. Colao, R. Fantoni, and V. Lazic, *Anal. Bioanal. Chem.*, **2006**, *385*, 272.
14. Z. Hu, Y. Liu, S. Gao, S. Hu, R. Dietiker, and D. Günther, *J. Anal. At. Spectrom.*, **2008**, *23*, 1192.
15. M. Guillong and D. Günther, *J. Anal. At. Spectrom.*, **2002**, *17*, 831.
16. Z. Wang, B. Hattendorf, and D. Günther, *J. Am. Soc. Mass Spectrom.*, **2006**, *17*, 641.
17. I. Rodushkin, M. D. Axelsson, D. Malinovsky, and D. C. Baxter, *J. Anal. At. Spectrom.*, **2002**, *17*, 1223.
18. C. O'Connor, B. L. Sharp, and P. Evans, *J. Anal. At. Spectrom.,* **2006**, *21*, 556.
19. M. Ohata, H. Yasuda, Y. Namai, and N. Furuta, *Anal. Sci.*, **2002**, *18*, 1105.
20. K. P. Jochum, B. Stoll, K. Herwig, and M. Willbold, *J. Anal. At. Spectrom.*, **2007**, *22*, 112.
21. Q. Z. Bian, J. Koch, H. Lindner, H. Berndt, R. Hergenröder, and K. Niemax, *J. Anal. At. Spectrom.*, **2005**, *20*, 736.
22. A. K. Souders and P. J. Sylvester, *J. Anal. At. Spectrom.*, **2010**, *25*, 975.
23. M. Guillong, I. Horn, and D. Günther, *J. Anal. At. Spectrom.*, **2003**, *18*, 1224.
24. J. Koch, A. von Bohlen, R. Hergenröder, and K. Niemax, *J. Anal. At. Spectrom.*, **2004**, *19*, 267.
25. Y. R. Luo and J. A. Kerr, in "*CRC Handbook of Chemistry and Physics*", ed. D. R. Lide, 86th ed., **2005**, Taylor & Francis, New York, Chap. 9, 54.